ADVANCED MATERIALS
www.advmat.de

Solid Polymer Electrolyte with Compatible Cathode-Electrolyte Interfacial Design Enabling Lithium Metal Batteries Operation at 4.8 V with Long Cycle Life

Jiajia Li, Haiman Hu, Jiufu Zhu, Xinyu Ma, Yin Hu, Haitao Zhang, Fengming Liu, Suojiang Zhang, and Xiaoyan Ji**

Lithium metal batteries (LMBs) with solid polymer electrolytes (SPEs) offer higher energy density and enhance safety compared to the Li-ion batteries that use a graphite anode and organic electrolytes. However, achieving long cycle life for LMBs while enabling the use of high-voltage cathodes required the compatibility between cathode-SPE, rather than focusing solely on the individual components. This study presente a dual-functional poly(ionic liquid) (PolyIL)-based material that simultaneously serves as an SPE matrix and a cathode binder, constructing a cathode-SPE interface with exceptional (electro)chemical compatibility owing to the high ionic conductivity and wide electrochemical stability window. Additionally, a modified cellulose acetate (CA)-based PolyIL substrate, enriched with C═O and —OH groups, is designed rationally and incorporated to assist the Li^+ migration, leveraging their highly negative charge, and enhancing the mechanical strength of the SPE. Furthermore, an in situ polymerization approach is employed to assemble the cells, improving the physical compatibility at the cathode-SPE interface. As a result, the Li||LFP cell demonstrate stable cycling beyond 1100 cycles, and the Li||NCM811 cell reliably operates at a high cut-off voltage of up to 4.8 V.

1. Introduction

The promise of forthcoming smart portable electronic devices, electronic vehicles (EVs), and power grids has spurred the relentless pursuit of lithium metal batteries (LMBs), owing to the high specific capacity (3860 mAh g^{-1}) and the low electrochemical potential (−3.04 V vs standard hydrogen electrode) of the Li metal.[1] Unfortunately, when using organic electrolytes, the uncontrollable side reactions and lithium dendrite growth result in safety hazards and a shortened cycle life during the cycling of LMBs. Additionally, the organic components, such as dimethyl carbonate (DMC), ethyl methyl carbonate (EMC), diethyl carbonate (DEC), propylene carbonate (PC), and ethylene carbonate (EC), which decompose at the operating voltages above 4.5 V due to their low oxidation potential, further exacerbates the challenges of using organic electrolytes in LMBs.

J. Li, H. Hu, X. Ji
Energy Engineering
Division of Energy Science
Luleå University of Technology
Luleå 97187, Sweden
E-mail: xiaoyan.ji@ltu.se

J. Zhu, H. Zhang
CAS Key Laboratory of Green Process and Engineering
Beijing Key Laboratory of Ionic Liquids Clean Process
Institute of Process Engineering
Chinese Academy of Sciences
Beijing 100190, P. R. China

X. Ma, Y. Hu
Jiangsu Engineering Laboratory of Novel Functional Polymeric Materials
Jiangsu
Key Laboratory of Advanced Negative Carbon Technologies College of Chemistry
Suzhou Key Laboratory of Soft Material and New Energy
College of Chemistry
Chemical Engineering and Materials Science
Soochow University
Suzhou 215123, P. R. China

F. Liu
Talga Technologies Limited
Luleå 972 35, Sweden

S. Zhang
Longzihu New Energy Laboratory
Zhengzhou
Institute of Emerging Industrial Technology
Henan University
Longzihu New Energy Laboratory, School of Energy Science and Technology
Henan University
Zhengzhou 450000, P. R. China
E-mail: sjzhang@ipe.ac.cn

The ORCID identification number(s) for the author(s) of this article can be found under https://doi.org/10.1002/adma.202501659

DOI: 10.1002/adma.202501659

Solid polymer electrolytes (SPEs), formed by a lithium salt and a polymer host, offer superior chemical stability, flame retardancy, and high mechanical strength, effectively suppressing side reactions and lithium dendrite growth. Additionally, their wide electrochemical stability window (ESW) offers the potential to be compatible with high-voltage cathodes, making SPEs a promising alternative to organic electrolytes in LMBs. Since the discovery of polyethylene oxide (PEO) as an SPE host in the 1970s[2] extensive research has been conducted on various polymer hosts, including poly(acrylonitrile) (PAN), poly(vinylidene fluoride) (PVDF), and polymethyl methacrylate (PMMA).[1] Despite considerable progress, the practical application of SPEs is still hindered by several challenges, including poor cycling stability (due to chemical and physical incompatibility), insufficient ionic conductivity, and incompatibility with high-voltage cathodes (due to electrochemical constraints). Furthermore, there are contradictions in achieving different targeted properties. For example, achieving high ionic conductivity requires either a semicrystalline polymer with low activation energy (E_a) or an amorphous polymer with low glass transition temperature (T_g), while these conditions often weaken the mechanical strength.[3] Thus, it is challenging to achieve both high ionic conductivity and high mechanical strength for a single SPE. Additionally, unlike organic electrolytes, SPEs do not naturally wet the electrode interfaces, resulting in poor physical compatibility, high interfacial resistance,[4] and sluggish Li^+ migration.[5]

In situ polymerization has emerged as one of the most effective and widely adopted approaches to optimize the physical compatibility between the cathode and SPE by directly polymerizing the SPE precursor solution on the cathode surface, forming a seamless, low-resistance interface. However, this approach fails to address (electro)chemical compatibility, leaving challenges such as interfacial side reactions, low antioxidant potential, and sluggish Li^+ migration unresolved. To realize long-term cycling stability, a more effective strategy is to integrate in situ polymerization with a comprehensive optimization of both the cathode and SPE, achieving a synergic effect across the physical, chemical, and electrochemical aspects. For example, if a polymer material can be used both in cathodes as a binder and SPEs as a host to enhance the performances of both components, supported by the "like dissolves like" principle, these materials with similar chemical structures will exhibit better compatibility. However, to our knowledge, no prior work has been done using such a novel strategy.

Identifying a proper polymer to serve as both a cathode binder and SPE host is crucial to implementing the above-mentioned strategy. For the aspect of the cathode, the ideal polymer binder should promote the Li^+ diffusion to decrease the resistance caused by the intrinsic interfaces within the cathode,[6] i.e., high ionic conductivity. Simultaneously, it should also exhibit strong adhesion and high oxidation potential. From the aspect of the SPE host, a promising polymer host needs to have high chemical stability, high ionic conductivity, high oxidation potential, and high flame retardancy. Therefore, the traditional cathode binders, such as PVDF,[7] carboxymethyl cellulose (CMC), xanthan gum (XG), guar gum (GG), sodium alginate (Alg), chitosan (CS), and carboxymethyl chitosan (C-chitosan),[8] cannot be chosen as an SPE host because of their poor ionic conductivity or low oxidation potential. Likewise, the common SPE hosts, such as PEO, PAN, PVDF, and PMMA, cannot work as a cathode binder due to their low adhesion, low oxidation potential, or limited chemical stability.

Poly(ionic liquid) (PolyIL), with high oxidation potential, high ionic conductivity, excellent chemical stability, strong adhesion, and intrinsic flame retardancy, is becoming a promising class of polymer material.[9] Previous investigations[10] have demonstrated that the PolyIL-based binder provides superior adhesive properties and favorable Li^+ diffusion within the cathode, as evidenced by the increased apparent Li^+ diffusion coefficient ($D_{Li}{}^+$). As an SPE host, PolyIL exhibits high oxidation potential and high ionic conductivity, making it adequate for high-voltage LMBs.

Furthermore, the inherent trade-offs in polymer properties make it difficult to develop high-performance SPEs using a single polymer host, including PolyIL-based materials. To address this, recent studies have introduced composite SPEs as a novel strategy, where the commercial polymer matrices (e.g., PEO, PVDF) are integrated into the PolyIL-based host through interpenetrating network architectures. For example, Lago et al.[11] developed an SPE by combining the poly(ethylene glycol) (PEG) networks with PolyIL-functionalized ceramic nanoparticles, which enhanced the ionic conductivity and widened ESW compared to the one without PEG. Similarly, Xie et al.[12] designed an SPE using a brush-structured PolyIL [PolyIL(TFSI)-FG_{brush}] with a PEO host, improving both ionic conductivity and mechanical strength. Despite their promising ESW values being higher than 5 V in the Li||stainless steel (SS) cells, these SPEs have demonstrated limited cycle life (< 500 cycles) in the Li||$LiFePO_4$ cells.[13] Such findings not only underscore the importance of composite SPEs but also illustrate the necessity of further enhancing the cathode-SPE interfacial engineering.

Based on the above analysis, this work proposed a novel strategy to simultaneously enhance the cathode-SPE interfacial compatibility and reduce the interfacial resistance by integrating a PolyIL-based material as both the cathode binder and the SPE constituent and coupling with in situ photopolymerization. Specifically, the PolyIL-based material was designed and optimized using 1-vinyl-3-butylimidazolium bis(trifluoromethyl-sulfonyl)imide (VBIMTFSI) and pentaerythritol tetraacrylate (PET4A) as crosslinkers to form a robust PolyIL host and serve as a solvent-free solution. To further enhance the ionic conductivity and the Li^+ transference number, lithium bis(trifluoromethanesulfonyl)imide (LiTFSI) and 1-ethyl-3-methylimidazolium bis(trifluoromethylsulfonyl)imide (EMIMTFSI) were incorporated. Additionally, a modified cellulose acetate (CA)-based PolyIL (CA-PolyIL), enriching with the polar hydroxyls (—OH^-) and carbonyl (C = O) groups, was incorporated as the matrix in preparing the SPE to enhance the mechanical strength, assist the Li^+ migration, and facilitate the redistribution of Li^+ on the lithium metal anode.[14] This study systematically evaluated the effect of compatibility between the cathode and the optimal SPE on the performance of the Li||$LiFePO_4$ and Li||$LiNi_{0.8}Co_{0.1}Mn_{0.1}O_2$ cells, with conventional PVDF binder-based cells included for comparison. Moreover, the underlying mechanisms driving the observed performance enhancement were elucidated, providing insights into the importance of material design and interfacial engineering for advancing high-performance LMBs.

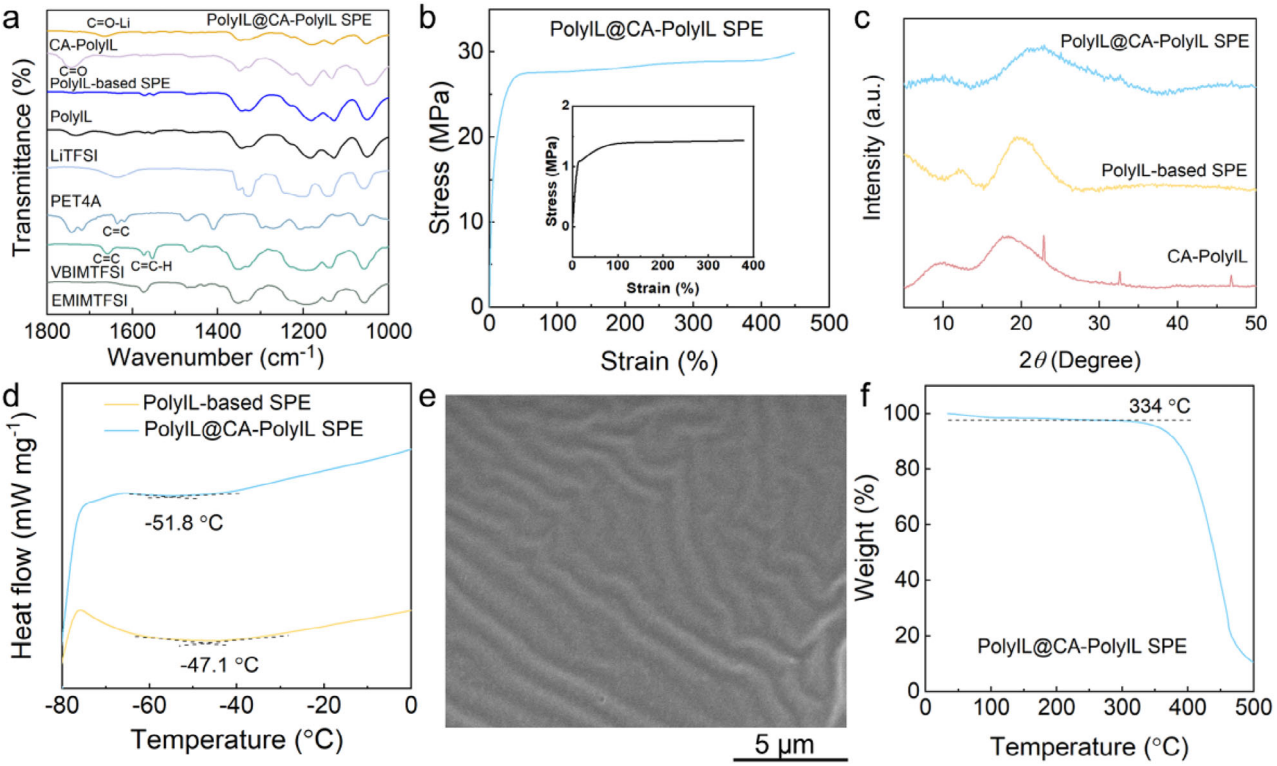

Figure 1. Characterization. a) FT-IR spectra. b) Strain–stress curves of PolyIL@CA-PolyIL SPE (inset: PolyIL-based SPE). c) XRD patterns. d) DSC curves. e) SEM image and f) TG curve of PolyIL@CA-PolyIL SPE.

2. Results and Discussion

The PolyIL-based materials were synthesized via one-step photopolymerization to fulfill three distinct roles: a cathode binder, a constitute of SPEs, and a blank SPE for comparison. The precursor solution, composed of VBIMTFSI, PET4A, Li-IL (LiTFSI dissolved in EMIMTFSI at 1.5 mol L^{-1}), and 2-hydroxy-2-methyl-1-phenylpropanone (HMPP) initiator, was homogenized by stirring in an argon-filled glove box, degassed to eliminate trapped air, and subsequently polymerized under the ultraviolet (UV)-curing (Figure S1, Supporting Information). Systematic optimization of the composition and polymerization time was conducted by evaluating the ESW and ionic conductivity (Figure S2, Supporting Information), with the experimental design detailed in Table S1 (Supporting Information). The optimal formulation was determined to consist of VBIMTFSI (1.045 g), PET4A (0.075 g), and Li-IL (0.840 g), with a polymerization time of 14 min.

The optimized PolyIL-based material was defined 1) as PolyIL-based SPE when employed as a free-standing SPE and 2) as PolyIL-based binder when integrated into the cathode. When the CA-PolyIL matrix was added to the PolyIL-based SPE precursor solution, the synthesized composite SPE was defined as PolyIL@CA-PolyIL SPE.

2.1. Characterization

The chemical composition of the synthesized PolyIL-based materials and SPEs was reflected by the Fourier transformation infrared (FT-IR) spectra. As shown in **Figure 1a**, the C═C stretching band at 1658.4 cm^{-1} and the C═C—H bond at 1469.4 cm^{-1} of the VBIMTFSI monomer almost disappeared, and the intensity of the C═C peak of PET4A at 1637.2 cm^{-1} weakened, indicating that the VBIMTFSI and PET4A monomers were successfully polymerized into PolyIL. This conclusion was further corroborated by the ^{1}H-nuclear magnetic resonance (NMR) spectra (Figure S3, Supporting Information), where the proportion of the —CH_2 signal in the PolyIL was reduced by 75%. Furthermore, after incorporating the Li-IL solution, all C═C peaks associated with VBIMTFSI and PET4A vanished, suggesting that the Li-IL solution promoted the cross-linking reaction, which was further confirmed by the molecular weight data listed in Table S2 (Supporting Information). The FT-IR spectra of the CA-PolyIL substrate with detailed illustrations are shown in Figure S4 (Supporting Information). The C═O stretching vibration in the PolyIL@CA-PolyIL SPE exhibited a blue shift compared to that of the pristine CA-PolyIL (1743.7 vs 1667.1 cm^{-1}), confirming the coordination interactions between Li^+ and the carbonyl oxygen atoms (Figure S5, Supporting Information), which provided an additional pathway for the Li^+ migration.[15] Additionally, the weakened C═C—H peak confirmed that a cross-linking reaction occurred between the PolyIL-based precursor solution and the CA-PolyIL matrix. This intermolecular cross-linking enhanced the tensile strength and elongation-at-break of the PolyIL@CA-PolyIL SPE. As illustrated in Figure 1b, the tensile strength of the PolyIL-based SPE was 1.4 MPa, with an elongation-at-break of 377.5%. In contrast, the PolyIL@CA-PolyIL SPE exhibited significantly improved tensile strength and elongation-at-break,

reaching 29.9 MPa and 448.4%, respectively. These enhanced mechanical properties are beneficial for suppressing lithium dendrite growth.

Furthermore, X-ray diffractometer (XRD) and differential scanning calorimetry (DSC) were applied to evaluate the crystallinity and T_g of SPEs. As depicted in Figure 1c, the PolyIL-based SPE displayed two broad diffraction peaks at the 2θ of 11.9° and 19.7°, suggesting a low proportion of intrinsic ordered structure. In contrast, the CA-PolyIL matrix exhibited high crystallinity, as evidenced by the diffraction peaks at the 2θ of 22.9°, 32.7°, and 46.8°. Upon combining these two, the crystallinity of the PolyIL@CA-PolyIL SPE was decreased, as evidenced by the almost disappearance of the characteristic diffraction peak at 11.9° and the substantial broadening of the peak at 19.7°. Additionally, as shown in Figure 1d, the PolyIL-based SPE exhibited a T_g of −47.1 °C, which further decreased to −51.8 °C after adding the CA-PolyIL matrix. These reductions in both crystallinity and T_g indicate that the PolyIL@CA-PolyIL SPE is more irregular and disordered, enhancing the Li^+ migration. The significantly improved mechanical strength and the reduced T_g highlight the key role of the CA-PolyIL matrix in achieving a balance between the kinetics of the Li^+ migration and the mechanical integrity through molecular-level structural engineering.

Scanning electron microscopy (SEM) was used to examine the morphology of SPEs. As demonstrated in Figure S6 (Supporting Information), the surface of the PolyIL-based SPE appeared rough and irregular, while the CA-PolyIL substrate showed a porous structure due to the volatilization of the NMP solvent. Notably, the PolyIL@CA-PolyIL SPE demonstrated a textured surface with wrinkles (Figure 1e), which resulted from the polymerization between the PolyIL-precursor solution and the CA-PolyIL matrix during UV curing. Energy dispersive spectroscopic (EDS) mapping (Figure S7, Supporting Information) confirmed the uniform elemental distribution throughout the SPE, indicating that the precursor solution effectively infiltrated into the CA-PolyIL matrix without phase separation, ensuring good contact between them.

Further, the thermal stability of SPEs was evaluated by thermogravimetric analysis (TGA) and flammability test. The PolyIL-based SPE and the PolyIL@CA-PolyIL SPE exhibited onset decomposition temperatures of 348 and 334 °C (Figure 1f; Figure S8, Supporting Information), respectively, which are comparable to the SPE systems reported in the literature (Table S3, Supporting Information), highlighting the exceptional thermal stability of the studied SPEs. The slightly lower onset decomposition temperature of PolyIL@CA-PolyIL was attributed to the CA-PolyIL substrate, exhibiting an onset decomposition temperature of 270 °C. Based on the extrapolation in the range of 334–348 °C, the content of CA-PolyIL in the PolyIL@CA-PolyIL SPE was estimated to be 10.8 wt%. The flammability test was conducted for both SPEs, together with the Celgard 2500 separator for comparison. As seen in Figure S9 and Videos S1–S3 (Supporting Information), the PolyIL-based and PolyIL@CA-PolyIL SPEs exhibit excellent thermal stability, with self-extinguishing times (SET) of less than 2 s. In contrast, the commercial Celgard 2500 separator ignited instantly and burned until fully consumed. According to the criterion that the materials with SET < 6 s g^{-1} are classified as nonflammable,[16] both PolyIL-based and PolyIL@CA-PolyIL SPEs meet the flame retardancy requirement, further enhancing the safety of LMBs.

2.2. Li^+ Migration Kinetics

Density functional theory (DFT) calculations were performed to elucidate the fundamental mechanisms underlying the Li^+ migration kinetics through the electrostatic potential (ESP) distribution and binding energy analysis, as shown in Figure S10 (Supporting Information), and **Figure 2a**. The computational results revealed that the —OH and C═O groups in CA-PolyIL possess the most negative electrostatic potential, serving as effective Lewis basic sites to promote the Li^+ dissociation from LiTFSI through strong coordination interactions. This facilitated more Li^+ coordination with the —OH and C═O groups, thereby establishing additional pathways for the Li^+ migration. Furthermore, incorporating the CA-PolyIL matrix strengthened the binding energy between the SPE and $TFSI^-$ from −78.54 to −84.55 kJ mol^{-1}, indicating a stronger $TFSI^-$ immobilization. These synergistic effects collectively contributed to an increased Li^+ transference number (t_{Li^+}) of 0.28 for PolyIL@CA-PolyIL (Figure 2b; Figure S11, Supporting Information), compared to ≈0.15 of the PolyIL-based SPE (Figure S12, Supporting Information).

Furthermore, the ionic conductivity (σ) of the PolyIL@CA-PolyIL SPE was calculated to be 0.12 mS cm^{-1} at room temperature and 1.20 mS cm^{-1} at 85 °C, compared to 0.05 and 0.76 mS cm^{-1} for the PolyIL-based SPE, respectively (Figure 2c; Figure S13, Supporting Information). The relevant electrochemical characterizations and notes on EMIMTFSI and Li-IL are provided in Figure S14 (Supporting Information), for further comparison. The activation energies (E_a) of the PolyIL-based SPE and the PolyIL@CA-PolyIL SPE were further determined to be 38.24 and 32.17 kJ mol^{-1}, respectively, implying that PolyIL@CA-PolyIL indeed possesses a lower Li^+ migration energy barrier than that of the PolyIL-based SPE (Figure 2d). This implication is in line with the aforementioned ESP results and t_{Li^+}, further suggesting that including CA-PolyIL facilitates the Li^+ migration.

The interfacial stability during the Li^+ plating/stripping cycling was investigated by determining the critical current density (CCD) of SPEs. As shown in Figure S15 (Supporting Information), the CCD of the PolyIL-based SPE was 0.2 mA cm^{-2}, indicating poor interfacial stability. In contrast, the PolyIL@CA-PolyIL SPE withstood a significantly higher CCD of 1.0 mA cm^{-2} (Figure 2e), due to its enhanced t_{Li^+} and superior strain-stress strength. Subsequently, the prolonged Li^+ plating/stripping process at 0.1 mA cm^{-2} was determined, as shown in Figure 2f and Figure S16 (Supporting Information), where the PolyIL@CA-PolyIL SPE maintained a stable process for over 3300 h with a minimal voltage polarization (80 mV), while the PolyIL-based SPE, despite showing initial cycling stability, experienced short circuit after 1369 h due to the interfacial degradation.

Furthermore, as one of the four indicators (t_{Li^+}, σ, exchange current density (j_0), the E_a of Li^+ diffusion) related to the kinetics of the Li^+ migration, the j_0 values of various cells were evaluated using the Tafel plots obtained from the fitting of the LSV curves (Figure 2g; Figure S17, Supporting Information), where the cell with the PolyIL-based SPE was included for comparison.

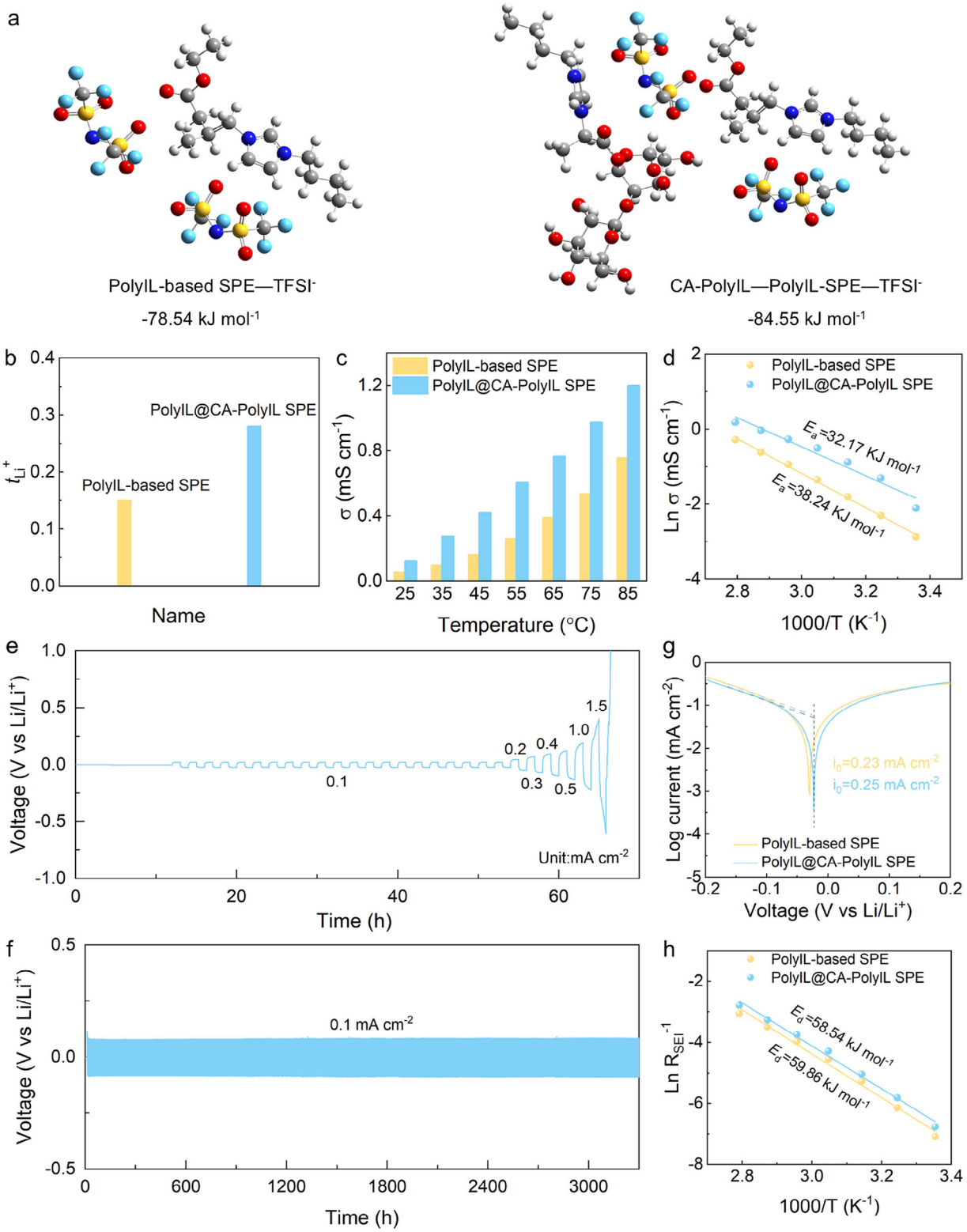

Figure 2. Li^+ migration dynamics. a) Binding energy between SPEs and $TFSI^-$. b) t_{Li^+}. c) σ as a function of temperature. d) Logarithms of σ versus temperature curves and E_a. Lithium plating/stripping curves with the PolyIL@CA-PolyIL SPE at e) various current densities and f) 0.1 mA cm^{-2}. g) Tafel plots. h) Li^+ diffusion energy barrier.

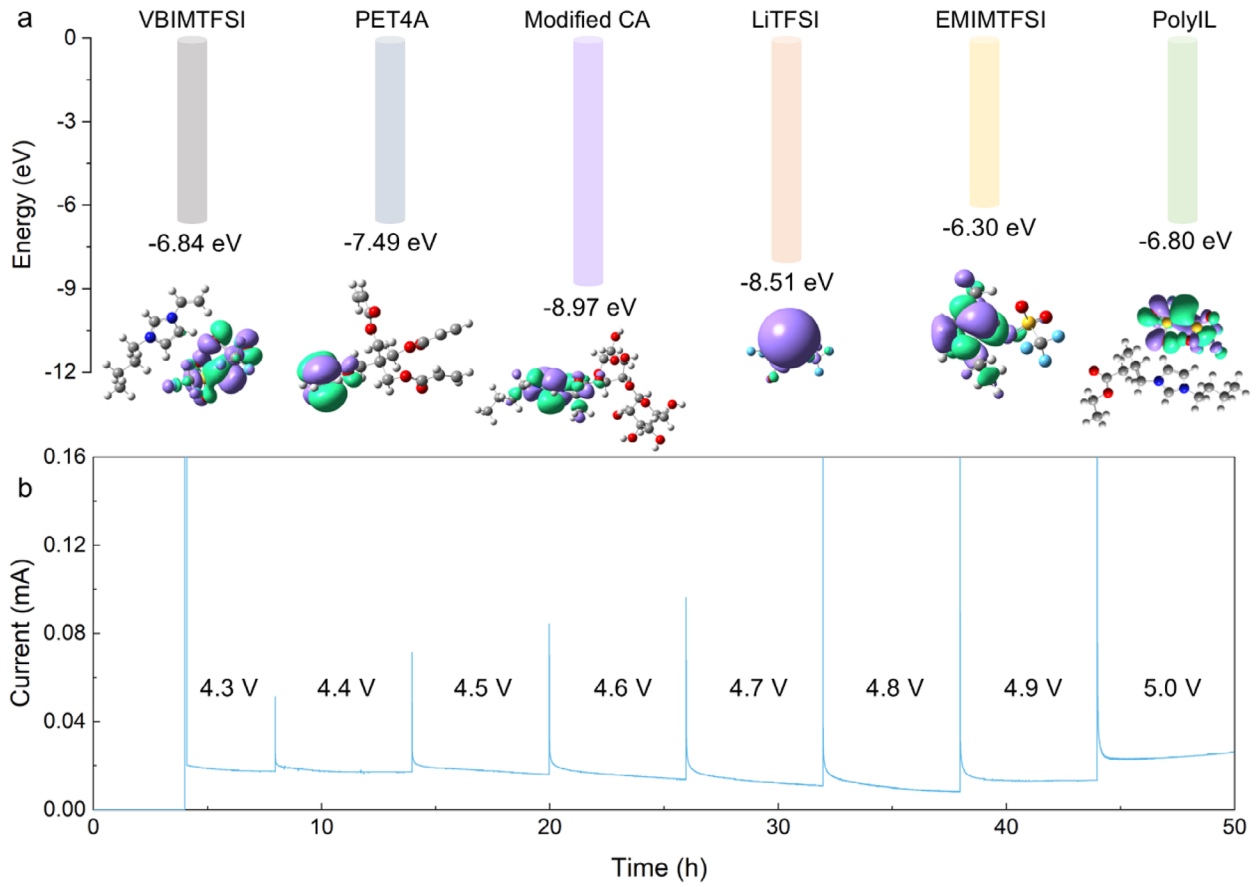

Figure 3. Oxidation stability. a) The HOMO energies. Purple, red, yellow, light blue, dark blue, silver, and dark gray balls stand for Li, O, S, F, N, H, and C atoms, respectively. b) Electrochemical floating test.

The cell with the PolyIL@CA-PolyIL SPE presented an increased j0 of 0.25 mA cm^{-2}, representing an 8.7% improvement over the PolyIL-based SPE (0.23 mA cm^{-2}). This improvement suggests a faster Li^+ migration at the interface of the solid electrolyte interphase (SEI) formed with the PolyIL@CA-PolyIL SPE. Simultaneously, the Li^+ diffusion energy barrier (E_d) through SEI was also determined by fitting the Nyquist plots from the Li||Li cells over a temperature range of 25 to 85 °C (Figure S18, Supporting Information). As referenced in Figure 2i, the E_d value for the cell with the PolyIL@CA-PolyIL SPE (58.87 kJ mol^{-1}) was lower than that for the cell with the PolyIL-based SPE (70.46 kJ mol^{-1}). This indicates an enhanced Li^+ diffusion capacity through the SEI with the PolyIL@CA-PolyIL SPE.

The lowest unoccupied molecular orbital (LUMO) energy levels of the components and PolyIL were calculated using DFT (Figure S19a, Supporting Information) to assess their electronic properties. A lower LUMO energy level indicates a greater ability to accept electrons, thereby promoting the chemical reduction reactions more readily.[17] Among the analyzed materials, CA-PolyIL exhibited the lowest LUMO energy level, suggesting its superior electron-accepting capability. This theoretical prediction was further validated through the reduction behavior of SPEs observed in the cyclic voltammetry (CV) curves (Figure S20, Supporting Information). The results showed a decomposition peak of $TFSI^-$ at −0.311 V in the PolyIL-based SPE, which shifted to −0.256 V in the PolyIL@CA-PolyIL SPE. This shift indicates that the incorporation of CA-PolyIL enhances the reduction of $TFSI^-$, promoting the formation of an SEI with an increased LiF content due to the presence of $TFSI^-$ in its molecular structure. The deconvoluted F1s X-ray photoelectron spectra (XPS) in Figure S19b–d (Supporting Information), further confirmed this conclusion. Based on the XPS analysis, the LiF content on the surface of the Li metal anode from the cell with the PolyIL-based SPE was estimated to be 1.06%, while it increased to 1.53% with the PolyIL@CA-PolyIL SPE. Furthermore, the SEM characterization of the cycled Li-metal surfaces revealed morphological differences: the PolyIL@CA-PolyIL SPE yielded a smooth and dendrite-free Li deposition morphology (Figure S21, Supporting Information), in contrast to the dendrite formation observed with the PolyIL-based SPE.

The oxidation stability of SPEs is crucial for their application in the high-voltage LMBs. Theoretically, the DFT calculations were conducted for all the components in the studied SPEs (**Figure 3a**). Among them, EMIMTFSI exhibits the highest HOMO energy level, indicating that all other components in the SPEs possess better oxidation stability than EMIMTFSI. As EMIMTFSI remains stable up to 4.7 V,[18] the oxidation stability of the studied SPEs will equal or exceed 4.7 V, making them compatible with the high-voltage cathodes. Practically, the oxidation stability of the PolyIL@CA-PolyIL SPE was determined through an

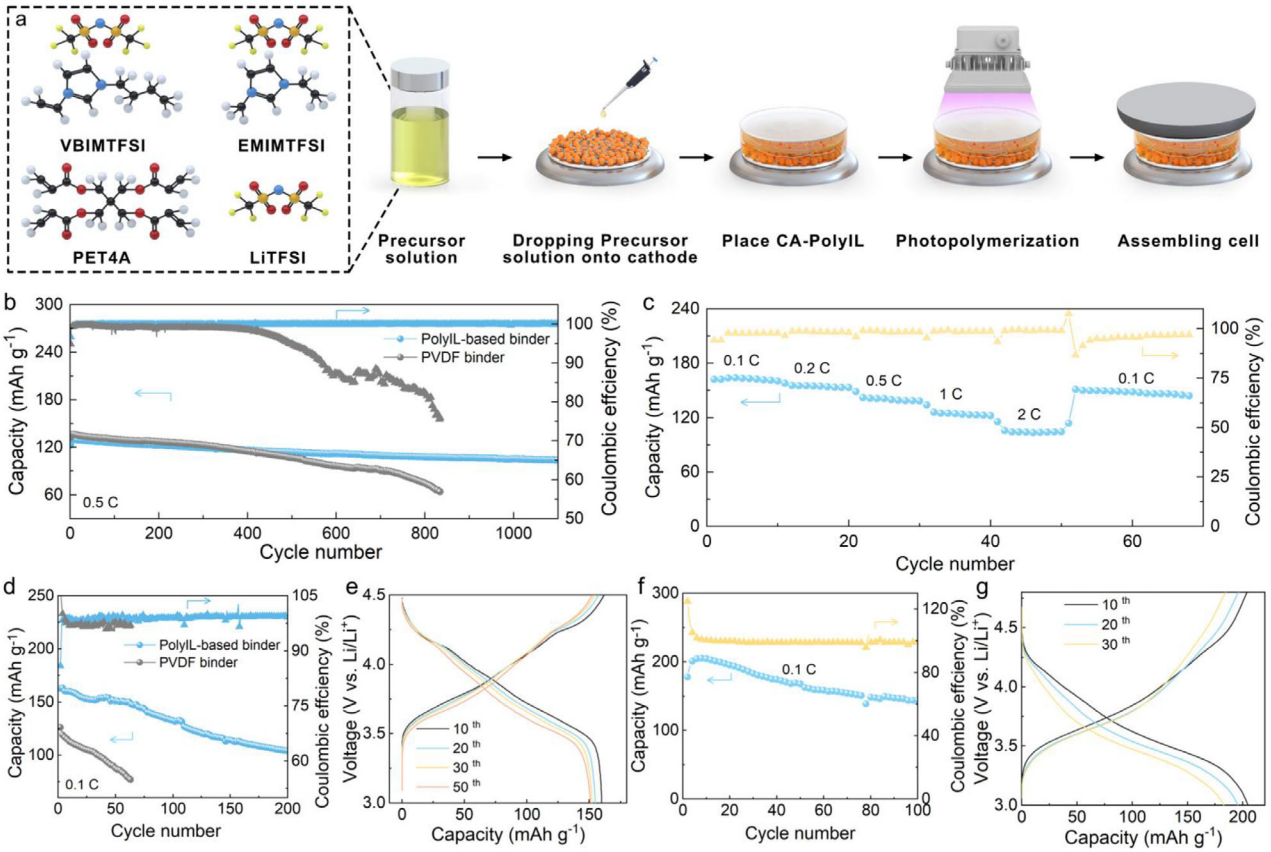

Figure 4. Electrochemical performance of coin cells. a) Schematic diagram illustrating the in situ engineering of LMBs. b) Cycling and c) rate performance of the Li||LFP cells. d) Cycling performance of the Li||NCM811 cells operated at 4.5 V. e) Charging/discharging curves of the Li||NCM811 cell with the PolyIL-based binder. f) Cycling performance of the Li||NCM811 cell with the PolyIL-based binder operated at 4.8 V and its g) charging/discharging curves.

electrochemical floating test, where the cell was paired with a $LiNi_{0.8}Co_{0.1}Mn_{0.1}O_2$ (NCM811) cathode (Figure 3b). The leakage current provides a direct measure of the oxidation stability.[19] The system maintained an exceptionally low leakage current (<0.04 mA) at an elevated potential of 5.0 V, significantly outperforming previously reported SPE systems (Table S4, Supporting Information).

In summary, the CA-PolyIL matrix is pivotal in optimizing the mechanical strength of the PolyIL-based SPE and facilitating the Li^+ migration, driven by the interactions of the C═O and —OH functional groups. Moreover, it promotes the formation of an SEI with an increased LiF content. These findings highlight the importance of molecular engineering in developing SPEs and demonstrate that composite SPE architectures can effectively overcome the traditional trade-offs between mechanical properties, ionic conductivity, and interfacial stability in the electrolyte design.

2.3. Effect of Cathode-SPE Compatibility on the Performance of Coin Cells

Using the PolyIL@CA-PolyIL SPE, both low-voltage Li||LFP and high-voltage Li||NCM811 cells were assembled (**Figure** 4a) to evaluate the impact of the cathode-SPE interfacial compatibility on the cell performance. The cell of Li||LFP with the PolyIL-based binder (Figure 4b) exhibited an initial discharge capacity of 122.9 mAh g^{-1} and retained 84.5% of its capacity after 1100 cycles at 0.5 C. Rate performance tests were conducted at the current densities ranging from 0.1C to 2C, where 1C equals 170 mAh g^{-1} (Figure 4c), showing that the cell retained 63.40% of its initial specific capacity at 2C compared to 0.1C. For the high-voltage Li||NCM811 cells (Figure 4d,e), operation at a cut-off voltage of 4.5 V delivered a high initial specific capacity of 145.5 mAh g^{-1}, with stable cycling performance over 200 cycles and a capacity retention of 63.9%. Furthermore, at an elevated cut-off voltage of 4.8 V (Figure 4f,g), the Li||NCM811 cell achieved a specific capacity of 178.1 mAh g^{-1} at 0.1C and retained 71.58% of its initial specific capacity after 100 cycles. For comparison, the performance of cells using the PVDF binder was evaluated. The Li||LFP cell delivered a specific capacity of 132.3 mAh g^{-1} but dropped to 64.1 mAh g^{-1} after 830 cycles, reflecting a poor capacity retention rate of 48.5% (Figure 4b). Similarly, the Li||NCM811 cell using the PVDF binder retained only 61.1% of its initial specific capacity after 60 cycle (Figure 4d).

It should be addressed that, attributed to the intrinsic high-voltage cathode degradation mechanisms evidenced by the dQ/dV analysis and CV results (Figures S22, Supporting Information), the cycling performance and capacity retention rate of

the Li||NCM811 cell remain suboptimal, while this study marks a significant step forward in understanding the cathode-SPE compatibility in LMBs, particularly under the challenging conditions of the high cut-off voltages.

2.4. Interfacial Compatibility Mechanism Analysis

In this section, the reasons and underlying mechanisms behind the cell performance enhancement were systematically analyzed, from the investigation of the physical properties of binders to the in-depth study of cathode and cell resistance changes during the cell charging/discharging process.

The adhesion between the binder and the current collector is a key factor in assessing the durability of the cathode. As demonstrated by the peeling test shown in Figure S23 (Supporting Information), the LFP cathode with the PolyIL-based binder maintained a steady peeling force of 0.6 N for ≈700 s, demonstrating superior flexibility and sustained adhesion. In contrast, the LFP cathode with the PVDF binder initially showed a higher peeling force of 1.2 N, which decreased to 0.7 N after 300 s and then failed rapidly ≈350 s.

Ion diffusion pathways are crucial for achieving uniform redox reactions in cathodes. To elucidate the ion diffusion within the cathodes, electrochemical impedance spectroscopy (EIS) was conducted for the symmetric cell (LFP|SPE|LFP) at 0% state of charge (SOC). The transmission line equivalent circuit model (TLM) for the Nyquist plots in **Figure 5a** was provided in Figure S23 (Supporting Information). Ogihara et al.[20] reported that the slope observed in the low-frequency region of the Nyquist plot, when projected onto the real axis and defined as ion resistance (R_{ion})/3, could be used to reflect the ion diffusion within the cathodes. The R_{ion}/3 values for the cathodes used in the PolyIL-based and PVDF binders were 75.4 and 135.7 Ω cm^2, respectively. The lower value of R_{ion}/3 for the PolyIL-based binder demonstrated its effectiveness in facilitating ion diffusion. This improvement is attributed to the cross-linking network structure formed by the VBIMTFSI and PET4A monomers as well as EMIMTFSI and LiTFSI in it, which creates a Li^+ diffusion bridge and thus significantly improves the ion diffusion and optimizes the electrochemical performance of the cells.

To intuitively assess the impact of the PolyIL-based binder on the Li^+ diffusion kinetics within cathodes, the Li^+ diffusion coefficient (D_{Li^+}) was estimated using CV and galvanostatic intermittent titration technique (GITT)[21] (Figures S25–S27, Supporting Information), where the LFP cathode with the PVDF binder was used as the reference for comparison. As shown in Figure 5b, the Li^+ diffusion rate within the LFP cathode using the PolyIL-based binder is higher than that using the PVDF binder. Meanwhile, the contact angle measurements between the precursor solution and the LFP cathode (Figure 5c; Figure S28, Supporting Information) reveal that the LFP cathode with the PolyIL-based binder exhibits superior wettability. This superior wettability, resulting from the shared components of the PolyIL-based binder and the precursor solution of the PolyIL@CA-PolyIL SPE, improves the compatibility between them.

The spatiotemporal evolution of chemical information at the cathode-SPE interface was monitored using in situ Raman spectroscopy (Figure 5d,e). The peaks at 1380 and 1740 cm^{-1} corresponded to the stretching vibrations of the C—F and C═C groups, respectively. In particular, the Raman peaks remained stable throughout the charging/discharging process, underscoring the superior interfacial compatibility between the cathode and SPE. This stability explains the enhanced cycling performance of the Li||LFP cells with the PolyIL-based binder. In contrast, for the cathode with the PVDF binder, the repeat of the appearance and disappearance of these peaks indicated that the cathode-SPE interface was dominated by the by-products from the $TFSI^-$ decomposition,[22] leading to the repeated dissolution and formation during the charging/discharging process. During the process, the C—F bond cleavage in PVDF at elevated temperatures during cycling triggered the reactions with LiTFSI, EMIMTFSI, and PolyIL, which was substantiated by the XPS analysis in the following section.[23]

The internal resistance of the Li||LFP cells after the first charging/discharging process was determined from the current–voltage (IV) pulses, as detailed in Figure S29 (Supporting Information). The results showed that the cell with the PolyIL-based binder achieved a low internal resistance (467.87 Ω), which was reduced to at least 60% compared to the PVDF binder (vs 813.34 Ω).

The EIS measurements were further conducted before cycling as well as after 20 and 50 cycles (Figure S30a–d, Supporting Information) to monitor the resistance changes during the cell operation. Meanwhile, the distribution of relaxation time (DRT) fitted from the Nyquist plots was used to quantitatively analyze the resistance evolution (Figure S30b,c,e,f, Supporting Information), where the integrated areas represented the resistance changes (Figure 5g). For the electrode-electrolyte contact impedance (R_c) in the high-frequency region, the cell with the PolyIL-based binder consistently exhibited lower R_c values both before cycling and after 50 cycles compared to the cell with the PVDF binder, indicating desirable electrode-electrolyte contact during cycling. In contrast, the R_c values of the cell with the PVDF binder fluctuated significantly during cycling, likely due to the decomposition of the PVDF binder. The peak in the 10^{-3} to 10^{-2} s range was ascribed to the evolution of the SEI (R_{SEI}). As shown in Figure 5g, the R_{CEI} value of the cell with the PolyIL-based binder exhibited a trend of initial increase, followed by a subsequent decrease; whereas in the cell with the PVDF binder, it exhibited the opposite trend, decreasing initially and then increasing. The different R_{SEI} behaviors suggested the variations of the SEI composition, which were further discussed in the XPS characterization section. The lower R_{ion} observed in the cell with the PolyIL-based binder also indicated higher ion diffusion capacity compared to the PVDF binder, as demonstrated in Figure 5a. Consequently, the cell with the PolyIL-based binder achieved superior Coulombic efficiency (>99.96% vs >93.80%, Figure 4b) than that used the PVDF binder. These results highlight the importance of cell engineering in optimizing battery performance. Figure 5i summarizes the proposed design strategy for improving the cell performance.

Finally, the XPS spectra were further used to analyze the surface of the NCM811 cathode after 50 cycles in the Li||NCM811 cells to examine the composition of the cathode electrolyte interphase (CEI) layer (Figure S31, Supporting Information). The characteristic peaks at 284.8 and 286.6 eV corresponded to the C—C and C—O bonds, respectively. Notably, the NCM811

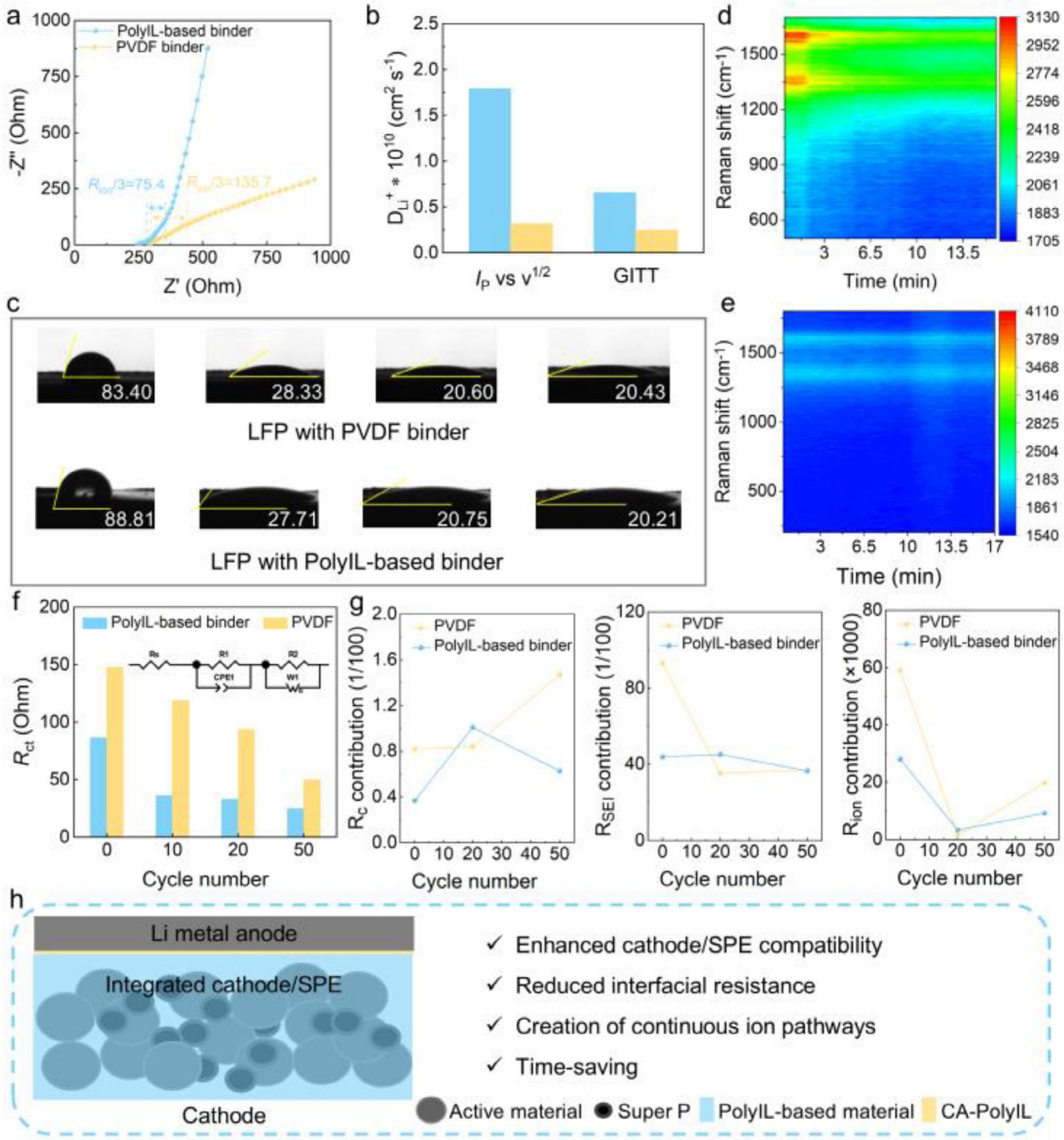

Figure 5. Cathode-SPE interfacial compatibility mechanism analysis. a) Nyquist plots of the cathode with the PVDF and PolyIL-based binders, in which solid symbols and solid lines represent experimental data and fitted curves based on TLM, respectively. b) Comparison of D_{Li}^{+} obtained through two methods. c) Contact angle of the LFP cathode with the PVDF or PolyIL-based binder and the PolyIL-based material precursor solution. In situ Raman spectroscopy of the Li||LFP cells used d) PVDF and e) the PolyIL-based binder during the first charging/discharging process. f) R_{ct} value after different cycles in the Li||LFP cells. g) The fitted peak areas for the Li||LFP cells with the PVDF and PolyIL-based binders. h) Advantages of the in situ assembly coin cell combined with the usage of the PolyIL-based binder/SPE.

cathode after the cycle with the PolyIL-based binder generated more C—O-containing components (20.47%) compared to the cell with the PVDF binder (10.40%), and the cell with the PVDF binder also exhibited a higher proportion of C-C-containing by-products (31.53% vs 13.93%). The oxygen-rich organic CEI stabilized the bulk phase of the NCM811 cathode, thereby enhancing the cycling performance (Figure 4d–g). Meanwhile, the presence of CO_3^{2-} in the C 1s XPS spectra from the NCM811 cathode surface with the PVDF binder and the high ratio of the C—F bond proved the reactions between PVDF and $TFSI^-$,

as previously inferred from the results of the in situ Raman spectroscopy.

3. Conclusion

In summary, this work proposed and demonstrated a novel strategy, where the same PolyIL-based material served as both an SPE constitute and a cathode binder, together with in situ polymerization, to improve the cathode-SPE interfacial compatibility. The incorporation of a modified CA-PolyIL substrate further enhances the ionic conductivity (0.05 to 0.12 mS cm^{-1} at room temperature (RT)), the Li-ion transference number (0.15 to 0.28), and the mechanical strength (1.4 to 29.9 MPa) of the SPE. The combined improvements in the Li^+ diffusion within the cathode, the SPEs performance, and the cathode-SPE compatibility enable the Li||LFP cells to achieve stable cycling for over 1100 cycles and allow the Li||NCM811 cells to operate at a high cut-off voltage of up to 4.8 V. This work represents a significant advancement in the exploration of the PolyIL-based materials for high-voltage LMBs and underscores the crucial role of the cathode-SPE compatibility in extending the cycle life of LMBs.

4. Experimental Section

Materials: $LiFePO_4$ (LFP), $LiNi_{0.8}Co_{0.1}Mn_{0.1}O_2$ (NCM811), super P, polyvinylidene fluoride (PVDF, weight-average molecular weight (M_w) ≈53400, powder), Celgard 2500, and aluminum (Al) foil (20.0 µm) were obtained from the Hefei Kejing, China. Lithium bis (trifluoromethylsulfonimide) (LiTFSI, battery grade) was bought from the Jiangsu Guotai Super Power New Materials Co., Ltd, China. EMIMTFSI (99.0%) and VBIMTFSI (99.0%) were from the Qingdao Aolike New Material Technology Co., Ltd, China. PET4A, NMP (AR), and HMPP (99.0%, initiator) were purchased from Sigma–Aldrich. CA (DS = 1.89) was supplied by the Sichuan Push Acetati Co., Ltd. 2-chloropropionyl chloride (95.0%) and n-butylimidazole (99.0%) were purchased from Braunway Technology. Deuterated dimethyl sulfoxide (DMSO-d6, 99.8%) and n,n-dimethylformamide (DMF, AR, 99.5%) were obtained from the Beijing InnoChem Science & Technology Co., Ltd. The Li metal anode with a diameter of 15.8 mm and thickness of 0.1 mm was bought from the China Energy Lithium Co., Ltd.

Preparation of PolyIL-Based Materials: PolyIL-based materials were prepared for the following purposes: i) to identify the optimal composition based on their electrochemical properties, ii) to use it as the binder in preparing the cathodes, iii) to indirectly use it (i.e., directly use its precursor solution) as one constituent in preparing the "targeted" SPE via in situ polymerization, and iv) to directly use as a free-standing SPE.

The preparation of PolyIL-based material was performed via a one-step photopolymerization, as illustrated in Figure S1 (Supporting Information). Briefly, LiTFSI was dissolved in EMIMTFSI, which was denoted as Li-IL. The mixture of VBIMTFSI, PET4A, HMPP, and Li-IL, which was termed as the PolyIL-based material precursor solution, was put in a glass bottle and stirred for 0.5 h in a glove box (H_2O/O_2 < 0.01 ppm) at RT. Then, the mixed solution was poured into a polytetrafluoroethylene (PTFE) mold with a diameter of 16.5 cm and depth of 0.1 mm, resting for 1 h to remove bubbles. The PTFE mold was then put on a heating plate at 40 °C, and after 0.5 h, a UV light (365 nm) was employed to initiate photopolymerization.

The component ratios in the PolyIL-based materials were optimized step by step, i) preliminarily optimizing the mass ratio of the two monomers (VBIMTFSI to PET4A) in forming PolyIL; ii) optimizing the mass ratio between (VBIMTFSI+PET4A) and the Li-IL solution under two LiTFSI concentrations (1.0 and 1.5 mol L^{-1}) in forming the PolyIL-based materials; iii) re-optimizing the mass ratio between VBIMTFSI and PET4A in a given Li-IL solution concentration (1.5 mol L^{-1}). Throughout the process, the mass of HMPP was set to be 0.1% of the total mass of two monomers in all experiments. The optimal ratios of the components, along with the polymerization time, were chosen based on the results of ESW and ionic conductivity (Figure S2, Supporting Information).

Preparation of CA-PolyIL Substrate: The method for preparing CA-polyIL was taken from the work by Zhang.[24] without any modifications. Specifically, the CA-PolyIL powders were dissolved in the NMP solution and stirred at RT for 24 h to form a uniform mixture solution. The solution was then cast onto a glass plate using a scraper and dried in a vacuum oven at 70 °C for 24 h. The prepared samples were cut into a diameter of 16 mm disk and then stored in the glove box.

Preparation of Free-Standing SPEs: The free-standing SPEs, termed the PolyIL@CA-PolyIL SPEs, were prepared by immersing the CA-PolyIL substrate in the PolyIL-based material precursor solution for 10 min to achieve full penetration. Subsequently, the UV light was used to initiate the photopolymerization at 40 °C.

Preparation of Free-Standing Cathodes: The active material (LFP/NCM811 power) and super P (80/10 wt.%) were mixed and ground for 0.5 h until a uniform powder was obtained. 10 wt.% optimal PolyIL-based material or PVDF binder was dissolved in NMP and stirred for 12 h to form the binder solution. The binder solution was then mixed with the obtained uniform powder to form a slurry, which was vigorously stirred overnight. After that, the uniform slurry was coated onto the Al foil using a scraper and dried at 110 °C under a vacuum overnight. The cathodes were then cut into 14 mm diameter disks and stored in the glove box.

Assembly of the Coin Cells Via In Situ Polymerization: The coin cells were assembled in the glove box using the prepared free-standing cathode (LFP/NCM811) and CA-PolyIL substrate, together with the optimal precursor solution. Briefly, a 30 µL precursor solution was dropped onto the cathode, followed by placing the CA-PolyIL substrate on the top. After 10 min, the UV light was used to initiate the photopolymerization for 14 min. Subsequently, the Li metal anode was aligned and placed on the CA-PolyIL substrate. A spring and spacer were added to ensure the proper contact and adjust the pressure. Finally, the positive cap was aligned, and the cell was sealed using a crimping machine. A 2025-type coin cell case was used with a sealing pressure of ≈35 bar.

Materials Characterization: The XRD patterns were obtained from a ray diffractometer (Rigaku, Smartlab) with Cu Kα radiation (40 kV, 40 mA). The microstructure and the distribution of elements were examined by SEM (JSM-7001F). The mechanical properties of SPEs were investigated by an electronic tensile machine (TA, Q800) with a tensile speed of 1 mm min^{-1}. The number-average molecular weight (M_n) and M_w of PolyILs and the molecular weight distribution (M_z/M_w) were determined by gel permeation chromatography (GPC, PL-GPC50, NYSE: A). TGA (STA7200RV, Hitachi High-Tech) was conducted to analyze the thermal stability. The FT-IR spectra were obtained using a Thermo Nicolet 380 spectrometer over the wavenumber range of 1000–1800 cm^{-1}. The chemical environments of SPEs were checked by the Raman spectrometer with an exciting laser of 532 nm (HR800 Raman spectrometer, Horiba Jobin-Yvon Ltd). XPS was performed using an ESCALAB 250Xi spectrometer.

For the peel test, a 10-mm-wide and 30-mm-long cathode sample was attached to 3M tape, and the peel strength of the cathode specimens was measured with a high-precision micromechanical test system (Delaminator Adhesion Test System; DTS Company, Menlo Park, CA, USA). By pulling the tape at a constant displacement rate of 100 µm s^{-1}, the applied load was continuously monitored, and the force-displacement plots were made.

Electrochemical Measurements: The electrochemical performances of the CR2025-type coin cells were detected by the CHI660E electrochemical workstation (Shanghai Chenhua Instrument Co., Ltd). The ionic conductivity of the SPEs was measured based on the stainless steel (SS)|SPE|SS cells by using EIS tests in the frequency ranging from 10^{-1} to 10^6 Hz and at temperatures from 25 to 85 °C and calculated with Equation (1):

$$\sigma = d/RS \quad (1)$$

where d is the thickness of the SPE, R presents the intrinsic impedance value obtained from the Nyquist plot (EIS tests), and S denotes the surface area of SS (1.95 cm^{-2} in this work).

The Nyquist plot from the cell cycles was also used for the DRT analysis. E_a was obtained by calculating the resistance at temperatures from 25 to 85 °C according to the Arrhenius law:

$$\sigma = A \exp\left(-E_a / (R_i T)\right) \tag{2}$$

where A is the conductivity pre-exponential factor, T is the absolute temperature, and R_i is the ideal gas constant.

The activation energy through SEI (E_d) was determined by calculating the resistance of Li|SPE|Li cells after 10 cycles at 0.1 mA cm^{-2}, and the results were fitted to the Arrhenius law.

$$R_{SEI}^{-1} = A \exp\left(-E_d / R_i T\right) \tag{3}$$

where R_{SEI} corresponds to the interface impedance between the electrode and SPE.

t_{Li^+} was determined by combining the measurements of alternating current impedance and direct current polarization using the Li|SPE|Li cells. Specifically, the polarization currents of the cell, including those of initial (I_0) and steady-state (Is), were recorded under a direct current polarization voltage of 50 mV (ΔV), and the interfacial resistances before (R_0) and after (Rs) polarization were tested by alternating the current impedance. Subsequently, t_{Li^+} was calculated from the Bruce-Vincent-Evans Equation (4).

$$t_{Li^+} = \frac{I_S\left(\Delta V - I_0 R_0\right)}{I_0\left(\Delta V - I_s R_s\right)} \tag{4}$$

ESW was analyzed by the floating test in the Li||NCM811 cells. The Tafel plots were measured across a voltage range from −0.2 to 0.2 V (vs Li/Li^+) in the Li|SPE|Li cells under a scan rate of 1 mV s^{-1} and then managed for linear fitting. The galvanostatic intermittent titration technique (GITT) tests were performed on the CHI660E with a current density of 0.1C and a relaxation time of 1 h per (20 min of operation) during the test. $D_{Li}{}^+$ was calculated by Equation (5).

$$D_{Li^+} = \frac{4}{\pi\tau}\left(\frac{m_B V_m}{M_B S_c}\right)^2\left(\frac{\Delta E_s}{\Delta E_\tau}\right)^2 \tag{5}$$

where τ (s) represents the relaxation time, which was set to be 20 min in this work, m_B (g) corresponds to the mass of the cathode, M_B (g mol^{-1}) represents the molar mass, S_c (cm^2, 1.53 cm^2 in this work) is the contact area of the electrode with the electrolyte, V_m (cm^3 mol^{-1}) corresponds to the molar volume of the cathode, ΔE_s represents the change in voltage due to the pulse, and ΔE_τ indicates the voltage difference for a constant-current planting/stripping process.

Meanwhile, $D_{Li}{}^+$ was also evaluated using the CV curves in the Li||LFP cells, following Equation (6):

$$I_P = 2.69 \times 10^5 A n^{(3/2)} C_0 D_{(Li^+)}{}^{(1/2)} \nu^{(1/2)} \tag{6}$$

where A, n, and C_0 are the surface area, charge transfer number, and the molar concentration of Li^+ for LFP, respectively, $\nu^{1/2}$ is the square root of the scan rates, and I_P is the anodic/cathodic peak currents.

The reduction behavior of SPEs was investigated by the CV curves of the Li||SPEs||Li cells from an open-circuit voltage to 0.1 V to identify the decomposition potential, and the scan rate was 0.1 mV S^{-1}. The dendrite suppression capability and the cycling performances of cells were evaluated on a LAND battery tester (CT-2001A, Wuhan Rambo Electronics Co., Ltd.) under different current densities.

Theoretical Simulations: In this study, the initial 3D structures of all molecules and ion pairs were constructed using GaussView 6.0. Given the significant proportion of PolyIL in the CA-PolyIL@PolyIL SPE, a chain segment model containing either one or three repeating units of PolyIL was selected as the computational object to better capture the structural and electronic properties of the polymer system.

The initial structures of all reactants and products were pre-optimized using the semi-empirical PM6 (Parameterized Model number 6) method. The PM6 method offers high computational efficiency and can rapidly generate reasonable initial conformations, providing a solid starting point for subsequent highly accurate calculations. Based on the PM6 pre-optimized structures, a full geometry optimization was further performed using the density functional theory (DFT) with the B3LYP functional and the 6–31G(d) basis set. B3LYP was a widely used hybrid functional that balances the computational accuracy and cost, while the 6–31G(d) basis set includes the polarization functions to better describe the electronic distribution within molecules.

After the geometry optimization, the frequency analysis was conducted for all stable structures to confirm the absence of the imaginary frequencies, ensuring that the obtained structures correspond to the local minima on the potential energy surface. Additionally, the frequency analysis results were used for the zero-point energy (ZPE) corrections to obtain more accurate energy data. Finally, the binding energies were calculated using the basis set superposition error (BSSE) correction method to account for weak interactions. All computations were performed using the Gaussian 16 software package.

Supporting Information

Supporting Information is available from the Wiley Online Library or from the author.

Acknowledgements

This work was carried out in the project within M-ERA.NET 3 with support from the European Union's Horizon 2020 research and innovation programme under grant agreement No. 958174 and Vinnova (Swedish Governmental Agency for Innovation Systems). X.J. thanks the Swedish Energy Agency and STINT (CH2019-8287), and Bio4Energy. S. Zhang acknowledges the Major Project of the National Natural Science Foundation of China (22393962). H.Z. would like to thank the National Natural Science Foundation of China (No. U22A20417) and Y.H. would like to thank the Natural Science Foundation of Jiangsu Province (BK20240805) for their support.

Conflict of Interest

The authors declare no conflict of interest.

Data Availability Statement

The data that support the findings of this study are available from the corresponding author upon reasonable request.

Keywords

binder, high-voltage, lithium metal battery, poly(ionic liquid), solid state electrolyte

Received: January 23, 2025
Revised: March 9, 2025
Published online: March 27, 2025

[1] J. Li, H. Hu, W. Fang, J. Ding, D. Yuan, S. Luo, H. Zhang, X. Ji, *Adv. Funct. Mater.* **2023**, *33*, 2303718.

[2] X. Tang, X. Xu, M. Bai, M. Zhang, H. Wang, Z. Wang, A. Shao, H. Wang, Y. Ma, *Adv. Funct. Mater.* **2023**, *33*, 2210465.
[3] a) D. Zhang, X. Meng, W. Hou, W. Hu, J. Mo, T. Yang, W. Zhang, Q. Fan, L. Liu, B. Jiang, L. Chu, M. Li, *Nano Res. Energy* **2023**, *2*, 9120050; b) X. Lu, Y. Wang, X. Xu, B. Yan, T. Wu, L. Lu, *Adv. Energy Mater.* **2023**, *13*, 2301746.
[4] a) T. Dai, S. Wu, Y. Lu, Y. Yang, Y. Liu, C. Chang, X. Rong, R. Xiao, J. Zhao, Y. Liu, W. Wang, L. Chen, Y. S. Hu, *Nat. Energy* **2023**, *8*, 1221; b) Y. Lin, M. Wu, J. Sun, L. Zhang, Q. Jian, T. Zhao, *Adv. Energy Mater.* **2021**, *11*, 2101612.
[5] a) J. Kim, K. Lee, J. W. Kim, S. Kweon, H. Moon, T. Yim, S. Kwak, S. Lee, *Nature Commun.* **2023**, *14*, 5721; b) J. Kim, J. Kim, S. Cho, N. Kim, S. Lee, *Nat. Commun.* **2022**, *13*, 2541; c) W. Zhu, J. Zhang, J. Luo, C. Zeng, H. Su, J. Zhang, R. Liu, E. Hu, Y. Liu, W. D. Liu, Y. Chen, W. Hu, Y. Xu, *Adv. Mater.* **2023**, *35*, 2208974.
[6] M. Dixit, W. Zaman, N. Hortance, S. Vujic, B. Harkey, F. Shen, W. Tsai, V. De Andrade, X. Chen, N. Balke, K. Hatzell, *Joule* **2020**, *4*, 207.
[7] H. Zhang, C. Li, G. Eshetu, S. Laruelle, S. Grugeon, K. Zaghib, C. Julien, A. Mauger, D. Guyomard, T. Rojo, N. Gisbert-Trejo, S. Passerini, X. Huang, Z. Zhou, P. Johansson, M. Forsyth, *Angew. Chem., Int. Ed.* **2020**, *59*, 534.
[8] Q. He, J. Ning, H. Chen, Z. Jiang, J. Wang, D. Chen, C. Zhao, Z. Liu, I. Perepichka, H. Meng, W. Huang, *Chem. Soc. Rev.* **2024**, *53*, 7091.
[9] X. Ma, J. Yu, Y. Hu, J. Texter, F. Yan, *Ind. Chem. Mater.* **2023**, *1*, 39.
[10] a) S. Vauthier, M. Alvarez-Tirado, G. Guzmán-González, L. Tomé, S. Cotte, L. Castro, A. Guéguen, D. Mecerreyes, N. Casado, *Mater. Today Chem.* **2023**, *27*, 101293; b) G. Pace, M. Le, R. Clément, R. Segalman, *ACS Energy Lett.* **2023**, *8*, 2781.
[11] N. Lago, O. Garcia-Calvo, J. Lopez-del-Amo, T. Rojo, M. Armand, *ChemSusChem* **2015**, *8*, 3039.
[12] Y. Ye, H. Wang, S. Bi, Y. Xue, Z. Xue, X. Zhou, X. Xie, Y. Mai, *J. Mater. Chem. A* **2015**, *3*, 18064.
[13] a) F. Chen, X. Wang, M. Armand, M. Forsyth, *Nat. Mater.* **2022**, *21*, 1175; b) Y. Sha, T. Yu, T. Dong, X. Wu, H. Tao, H. Zhang, *ACS Appl. Energy Mater.* **2021**, *4*, 14755; c) L. Yu, L. Yu, Q. Liu, T. Meng, S. Wang, X. Hu, *Adv. Funct. Mater.* **2022**, *32*, 2110653.
[14] C. Chang, S. Chung, A. Manthiram, *Adv. Sustainable Syst.* **2017**, *1*, 1600034.
[15] J. Zhang, J. Zhao, L. Yue, Q. Wang, J. Chai, Z. Liu, X. Zhou, H. Li, Y. Guo, G. Cui, L. Chen, *Adv. Energy Mater.* **2015**, *5*, 1501082.
[16] Q. Zhang, X. Zhang, L. Hou, S. Sun, Y. Zhan, J. Liang, F. Zhang, X. Feng, B. Li, J. Huang, *Adv. Energy Mater.* **2022**, *12*, 2200139.
[17] S. He, Y. Chen, J. Fang, Y. Liu, Z. Lin, *Chem. Soc. Rev.* **2025**, *54*, 2154.
[18] Q. Li, J. Jiang, G. Li, W. Zhao, X. Zhao, T. Mu, *Sci. China Chem.* **2016**, *59*, 571.
[19] Y. Liu, H. Zou, Z. Huang, Q. Wen, J. Lai, Y. Zhang, J. Li, K. Ding, J. Wang, Y. Lan, Q. Zheng, *Energy Environ. Sci.* **2023**, *16*, 6110.
[20] N. Ogihara, S. Kawauchi, C. Okuda, Y. Itou, Y. Takeuchi, Y. Ukyo, *J. Electrochem. Soc.* **2012**, *159*, A1034.
[21] Z. Geng, Y. Chien, M. Lacey, T. Thiringer, D. Brandell, *Electrochim. Acta* **2022**, *404*, 139727.
[22] T. Ha, H. Li, X. Wang, L. O'Dell, M. Forsyth, C. Pozo-Gonzalo, P. Howlett, *ACS Appl. Energy Mater.* **2021**, *4*, 434.
[23] a) Z. Zhu, S. Tang, J. Yuan, X. Qin, Y. Deng, R. Qu, G. M. Haarberg, *Int. J. Electrochem. Sci.* **2016**, *11*, 8270; b) X. Zhao, S. Niketic, C. Yim, J. Zhou, J. Wang, Y. Abu-Lebdeh, *ACS Omega* **2018**, *3*, 11684.
[24] Y. Cheng, X. Zhang, C. Yin, J. Zhang, J. Yu, J. Zhang, *Macromol. Rapid Commun.* **2021**, *42*, 2000494.